UC Berkeley
UC Berkeley Previously Published Works

Authors

Peverati, Roberto
Platt, Sean P
Attah, Isaac K
et al.

Nucleophilic Aromatic Addition in Ionizing Environments: Observation and Analysis of New C–N Valence Bonds in Complexes between Naphthalene Radical Cation and Pyridine

Roberto Peverati,[a,b] Sean P. Platt,[c] Isaac K. Attah,[c] Saaudallah G. Aziz,[d] M. Samy El-Shall*[c] and Martin Head-Gordon* [a,b]

[a]Department of Chemistry, University of California, Berkeley, California 94720
[b]Chemical Sciences Division, Lawrence Berkeley National Laboratory, Berkeley, California 94720
[c]Department of Chemistry, Virginia Commonwealth University, Richmond, VA 23284
[d]Department of Chemistry, Faculty of Science, King Abdulaziz University, Jeddah 21589, Saudi Arabia

Abstract

Radical organic ions can be stabilized by complexation with neutral organics via interactions that can resemble chemical bonds, but with much diminished bond energies. Those interactions are a key factor in cluster growth and polymerization reactions in ionizing environments such as regions of the interstellar medium and solar nebulae. Such radical cation complexes between naphthalene (Naph) and pyridine (Pyr) are characterized using mass-selected ion mobility experiments. The measured enthalpy of binding of the $Naph^{+\bullet}(Pyr)$ heterodimer (20.9 kcal/mol) exceeds that of the $Naph^{+\bullet}(Naph)$ homodimer (17.8 kcal/mol). The addition of 1-3 more pyridine molecules to the $Naph^{+\bullet}(Pyr)$ heterodimer gives 10-11 kcal/mol increments in binding enthalpy. A rich array of $Naph^{+\bullet}(Pyr)$ isomers are characterized by electronic structure calculations. The calculated Boltzmann distribution at 400 K yields an enthalpy of binding in reasonable agreement with experiment. The global minimum is a distonic cation formed by Pyr attack on $Naph^{+\bullet}$ at the α-carbon, changing its hybridization from sp^2 to distorted sp^3. The measured collision cross section in helium for the $Naph^{+\bullet}(Pyr)$ heterodimer of 84.9±2.5 $Å^2$ at 302 K agrees well with calculated angle-averaged cross sections (83.9 – 85.1 $Å^2$ at 302 K) of the lowest energy distonic structures. A remarkable 16 kcal/mol increase in the binding energy between $Naph^{+\bullet}(Pyr)$ and $Bz^{+\bullet}(Pyr)$ (Bz is benzene) is understood by energy decomposition analysis. A similar increase in binding from $Naph^{+\bullet}(NH_3)$ to $Naph^{+\bullet}(Pyr)$ (as well as between $Bz^{+\bullet}(NH_3)$ and $Bz^{+\bullet}(Pyr)$) is likewise rationalized.

INTRODUCTION

Polycyclic aromatic hydrocarbons (PAHs) and nitrogen heterocycles (PANHs) are found in many environments, including under ionizing conditions in radiation chemistry and flames.[1,2] In space, PAHs and PANHs and their ions contain a large fraction of the organic carbon in interstellar clouds.[3-5] With low ionization energies and high proton affinities, these compounds can be charge and proton sinks, and the corresponding ions can serve as catalysts, provide nucleation centers for clusters, dust grains and polymers, and form carbonaceous mantles on silicate grains and ices.[6-8] Their large π systems can also serve as theoretical models for conjugated organic semiconductors and graphene.[9,10] The formation of PAHs and PANs can also involve ion chemistry, as observed in ionic association and polymerization reactions.[11-21]

In ionizing environments, PAH$^{+\bullet}$ and PANH$^{+\bullet}$ radical cations can interact with neutral PAH and PANH molecules. In fact, their dimers may contribute to interstellar IR bands.[5,9] These adducts entail three different types of structures and interactions: parallel π stacked dimers, that allow intermolecular charge transfer resonance and dispersion interactions; perpendicular L or T-shaped structures bonded by non-covalent electrostatic interactions; and linear twisted propeller-shaped adducts with covalent C-N bonds. Parallel π stacked homodimers are formed from benzene (Bz) (i.e. Bz$^{+\bullet}$(Bz)), naphthalene (Naph) (i.e. Naph$^{+\bullet}$(Naph)) and larger PAHs, with dissociation energies between 16 and 20 kcal/mol, including charge transfer resonance contributions of about 7 kcal/mol.[22-25] In larger PAHs, intramolecular charge delocalization can decrease intermolecular charge transfer, but increasing dispersion forces compensate, keeping the bond energy in the range of 16-20 kcal/mol for homodimers from Bz$^{+\bullet}$(Bz) to coronene$^{+\bullet}$(coronene).[22-24] Dissociation energies of PAH heterodimers may be significantly smaller: for example in the Naph$^{+\bullet}$(Bz) heterodimer, where the difference in the ionization energies of naphthalene and benzene is 1.1 eV, the binding energy has been recently measured as only 8 ±1 kcal/mol.[25]

Little is known about the chemistry and the nature of interaction in ionized PAH/PANH cross-adducts where a covalent C-N bond with potentially large dissociation energy may form. We have examined the prototype Bz$^{+\bullet}$(Pyr) and Bz$^{+\bullet}$(Pyrim) (Pyrim denotes pyrimidine) adducts that can form various non-covalent and covalently bonded isomers.[13,21] The ionization energies of benzene (9.24 eV), pyridine (9.26 eV) and pyrimidine (9.30 eV) are nearly equal, suggesting that Bz$^{+\bullet}$(Pyr) and Bz$^{+\bullet}$(Pyrim) may form parallel charge transfer complexes similar to Bz$^{+\bullet}$(Bz). However, we instead found that the most

stable isomer of Bz$^{+\bullet}$(Pyr) includes a covalent C–N bond, and has a dissociation enthalpy that we determined experimentally as > 33 kcal/mol, and computationally as 34.9 kcal/mol.[13] Very recently, we found that Bz$^{+\bullet}$(Pyrim) corresponds to two families of covalent and non-covalent isomers characterized by two ion mobility peaks corresponding to small and large collision cross sections in helium (67.7±2.2 Å^2 and 76.0±1.8 Å^2, respectively) consistent with two types of compact covalent and extended non-covalent structures, respectively.[21] DFT calculations at the M06-2X/6-311++G** level showed the most stable Bz$^{+\bullet}$(Pyrim) isomer contains a covalent C-N bond with a binding energy of 49.7 kcal/mol and a calculated collision cross section of 69.2 Å^2, in excellent agreement with the value obtained from the higher mobility peak observed experimentally.[21] Forming the C-N covalent bond displaces a hydrogen atom from a C-H bond of the benzene cation which is transferred to the second pyrimidine nitrogen atom, thus preserving the pyrimidine π system and yielding the most stable Bz$^{+\bullet}$(Pyrim) isomer. The calculations also show less stable non-covalent electrostatically bonded perpendicular isomers of Bz$^{+\bullet}$(Pyrim) with a binding energy of 19 kcal/mol and a calculated collision cross section of 74.0 - 75.0 Å^2 in excellent agreement with the value obtained from the lower mobility peak observed experimentally.[21]

The cation complexes Bz$^{+\bullet}$(Pyr) and Bz$^{+\bullet}$(Pyrim) formed between benzene radical cation and pyridine or pyrimidine are examples of stable distonic radical ions where (i) the charge and radical sites are spatially separated, and (ii) they may be formally derived from ionization of a neutral zwitterionic species, though such a species itself may not be stable. The addition of pyridine to the benzene cation ring yields a sigma complex that is also distonic: the closed shell pyridine N carries the charge, while the radical is delocalized around 5 sp^2 hybridized atoms of the former benzene ring. Remarkably, this complex is bound by a lower limit of 33 kcal/mol according to experimental estimates, making it much more strongly bound than the benzene radical cation-ammonia complex that has also been studied experimentally.[26-28] Why is the binding energy so much larger in the benzene-pyridine radical cation complex? What should be expected if we substitute benzene for naphthalene? More generally, what are the driving forces that stabilize these sigma complexes? These are some of the questions that we will be concerned with in this paper.

We address these issues in the context of a combined experimental and computational study of a new set of distonic complexes between the naphthalene radical cation and pyridine. The experiment utilizes the mass-selected ion mobility to determine the sequential binding energies of pyridine molecules to the naphthalene radical cation (i.e. Naph$^{+\bullet}$(Pyr)$_n$, with n =1-4) by equilibrium thermochemical measurements as well as the collision cross-section of the

Naph$^{+\bullet}$(Pyr) adduct in helium to obtain structural information on the gas phase conformation of the adduct. The calculations indicate that a variety of conformers are in equilibrium with each other under the experimental conditions. The experimental and computational results suggest a binding energy of over 20 kcal/mol, much stronger than a typical electrostatic ion-molecule complex. Experimental and computational values are also obtained for the coordination of an additional pyridine molecule to the Naph$^{+\bullet}$(Pyr) adduct. We find that the binding energy of the second pyridine is significantly smaller (unlike for example, the recently reported case of the Naph$^{+\bullet}$(Bz) complex, where coordination of a second benzene molecule carried the same binding energy as the first).[25] Computations suggest that the second pyridine in Naph$^{+\bullet}$(Pyr)$_2$ is not directly bonded to the naphthalene radical cation.

We also report electronic structure calculations that compare the benzene$^{+\bullet}$(pyridine) and naphthalene$^{+\bullet}$(pyridine) systems, as well as calculations on the benzene$^{+\bullet}$(ammonia) and the not-yet-experimentally measured naphthalene$^{+\bullet}$(ammonia) cation. These results show that the benzene$^{+\bullet}$(pyridine) complex is in fact bound by over 40 kcal/mol, and the naphthalene-ammonia cation complex is bound by only 12 kcal/mol. The C-N bond lengths are similar for all complexes, and we are therefore left with a puzzle. What is the origin of the more than three-fold range of binding energies that are seen across these four complexes? These results were rationalized using energy decomposition analysis (EDA) of the binding energies to unravel the remarkable differences between these four complexes.

EXPERIMENTAL SECTION

The experiments were performed using the VCU mass-selected ion mobility spectrometer (Schematic is given in Figure S1, Supporting Information). The details of the instrument can be found in several publications[15,21,25] and only a brief description of the experimental procedure is given here. The essential elements of the apparatus are jet and beam chambers coupled to an electron ionization source, a quadrupole mass filter, a drift cell, and a second quadrupole mass spectrometer. Mass-selected $C_{10}H_8^{+\bullet}$ ions (generated by electron impact ionization of naphthalene vapor) are injected (in 20 –30 μsec pulses) into the drift cell containing 1.0 Torr helium and 0.10 - 0.35 Torr of pyridine (C_5H_5N) vapor. The temperature of the drift cell can be controlled to better than ±1K using six temperature controllers. The reaction products can be identified by scanning a second quadrupole mass filter located coaxially after the drift cell. The injection energies used in the experiments (10–12 eV laboratory frame, depending on the pressure in the drift cell) are slightly above the

minimum energies required to introduce the naphthalene ions against the counter flow of the gas escaping from the cell. Most of the ion thermalization occurs outside the cell entrance by collisions with the helium atoms and pyridine molecules escaping from the cell entrance orifice. At a cell pressure of 0.2 Torr, the number of collisions that the naphthalene ion encounters within the 1.5 millisecond residence time inside the cell is about 10^4 collisions, which is sufficient to ensure efficient thermalization of the ions. The ion intensity ratio $C_{10}H_8^{+\bullet}(C_5H_5N)/C_{10}H_8^{+\bullet}$ is measured from the ion intensity peaks as a function of decreasing cell drift field corresponding to increasing reaction time, and equilibrium is achieved when a constant ratio is obtained. Equilibrium constants are then calculated from $K = [I(C_{10}H_8^{+\bullet}(C_5H_5N))/I(C_{10}H_8^{+\bullet})$ P(pyridine)] where I is the ion intensity taken from the mass spectrum and P(pyridine) is the partial pressure of pyridine in the drift cell. All the equilibrium experiments at different temperatures are conducted at correspondingly low drift fields and long residence times. The measured equilibrium constant is independent of the applied field across the drift cell in the low field region. The equilibrium constant measured as a function of temperature yields $\Delta H°$ and $\Delta S°$ from the van't Hoff equation [ln K = -$\Delta H°/RT + \Delta S°/R$].

For the mobility measurements, the neutral naphthalene and naphthalene-pyridine clusters are generated in the source chamber by supersonic pulsed adiabatic expansion.[29,30] During operation, a vapor mixture consisting of 230 Torr pyridine (C_5H_5N) (Aldrich, 99.9%) and 3.9 Torr naphthalene ($C_{10}H_8$) (Aldrich, ≥ 99%) in 5100 Torr helium (ultrahigh purity, Airgas 99.99%) is expanded through a conical nozzle (500 μm in diameter) in pulses of 300-400 μs duration at a repetition rate of 100 Hz. The jet is skimmed and passed into the second chamber, which is maintained at 2×10^{-6} Torr, where the clusters are ionized by 70 eV electrons. The ions are injected into the drift cell containing 1.0 Torr helium at different temperatures (200-300 K) using injection energy of 12.8 eV (lab frame). Mobility measurements are made by injecting a narrow pulse of ions into the drift cell.[29,30] The ion gate located just prior to the cell entrance (see Figure S1, Supporting Information) chops the pulse to a narrow, 30 to 50 μs wide packet, which enters the drift cell. As the ions are injected into the drift cell, the injection energy is dissipated by collisions with the helium buffer gas. The injection energies used in all the experiments are slightly above the minimum energies required to introduce the ions into the cell against the helium flow. Upon exiting the cell, the ions are collected and refocused into the second quadrupole for analysis and detection. The signal is collected on a multichannel scalar with the zero time for data acquisition set to the

midpoint of the ion gate trigger. The measured mobilities at different temperatures are used to calculate average collision cross sections (Ωs) for the ion with the helium buffer gas.[29,30]

COMPUTATIONAL SECTION

For the identification of structural minima, we used a methodology that combines quenching ab-initio molecular dynamics (QAIMD) starting from random initial orientations, followed by gradient-based local optimizations with density functional theory (DFT) using the ωB97X-V exchange-correlation functional[31] and the cc-pVTZ basis set.[32] This functional is known to be quite accurate for intermolecular interactions, as well as bonded interactions.[31] For validation purposes, additional single point energy results have been obtained using the B3LYP,[33-35] M06-2X,[36] and M11 functionals,[37] as well as with more advanced wave function techniques such as Møller-Plesset perturbation theory (MP2),[38] spin-component-scaled MP2 (SCS-MP2),[39] and orbital-optimized opposite spin MP2 (O2).[40] Despite a severe underestimation of the energy of some of the distonic structures with the popular B3LYP functional, all the modern DFT methods provide results that are in good agreement with the advanced wave function methods. For this reason, we report only the results obtained with the ωB97X-V functional, but we need to stress the need for caution when the popular B3LYP functional is used to calculate complex interaction in systems with distonic character. The newest version[41,42] of the absolutely localized molecular orbital energy decomposition analysis (ALMO-EDA)[43-46] was used to analyze the components of the bonds using the ωB97X-V functional and the pc3 basis set.[47,48] This version of the ALMO-EDA is applicable to both weak and strong interactions: indeed with an additional term for spin-coupling, it has been applied to chemical bonds.[49,50] All calculations were performed with the Q-Chem 4 quantum chemistry code.[51]

RESULTS AND DISCUSSION

Experimental Binding Enthalpy and Entropy Changes

Figure 1(A) displays the mass spectra obtained following the injection of the mass-selected naphthalene cation ($C_{10}H_8^{+\bullet}$) into the drift cell pure helium or helium-pyridine (C_5H_5N) gas mixtures. In 0.78 Torr helium at 296 K, the naphthalene$^{+\bullet}$.water complex is formed due to the presence of water vapor impurity in the drift cell. In the presence of 0.09 Torr C_5H_5N vapor in the drift cell at 310 K, the naphthalene ion signal disappears as the naphthalene$^{+\bullet}$(pyridine) heterodimer (Naph$^{+\bullet}$(Pyr) = $C_{10}H_8^{+\bullet}$(C_5H_5N)) is formed as shown in Fig. 1(A)-b along with a small intensity of the Naph$^{+\bullet}$(Pyr)$_2$ cluster formed by the second

addition of pyridine into the Naph$^{+\bullet}$(Pyr) adduct. Although no dissociation products of the naphthalene ion are observed (Fig. 1(A)) consistent with the low injection energy used, the observation of the small ion intensity of the protonated pyridine dimer H$^+$(pyridine)$_2$ suggests direct ionization of a small amount of the pyridine molecules in the cell by the injection energy. The pyridine ions are generated at early times followed by proton transfer to the neutral pyridine molecules generating protonated pyridine (H$^+$pyridine) which adds a neutral molecule to form the observed proton-bound pyridine dimer (H$^+$(pyridine)$_2$). The H$^+$(pyridine)$_2$ is not in equilibrium with the Naph$^{+\bullet}$ or the Naph$^{+\bullet}$(Pyr) ions, and therefore it has no effect on the equilibrium between the Naph$^{+\bullet}$ reactant and the Naph$^{+\bullet}$(Pyr) product.[52,53]

As the temperature of the drift cell increases, the ion intensity of the Naph$^{+\bullet}$(Pyr)$_2$ cluster decreases and eventually disappears (Fig. 1(A)-c at 378 K) indicating that the second pyridine molecule is weakly attached to the Naph$^{+\bullet}$(Pyr) adduct. As the temperature increases further, the intensity of the Naph$^{+\bullet}$(Pyr) adduct decreases as it dissociates to the naphthalene radical cation and neutral pyridine, and at 468 K, the ion intensity ratio of Naph$^{+\bullet}$(Pyr)/ Naph$^{+\bullet}$ decreases to about 0.1.

Figure 1(B) displays the mass spectra obtained at lower temperatures. As the temperature decreases, the equilibrium shifts to higher clusters as further pyridine molecules are attached to the Naph$^{+\bullet}$(Pyr) adduct. At the lowest possible temperature (223 K), the ion signal of the Naph$^{+\bullet}$(Pyr) adduct disappears as up to three pyridine molecules are attached to the adduct. At such low temperatures pyridine is also attached to the protonated dimer in a different reaction channel forming H$^+$(pyridine)$_3$ as shown in Figs 1(B)-d and 1(B)-e.

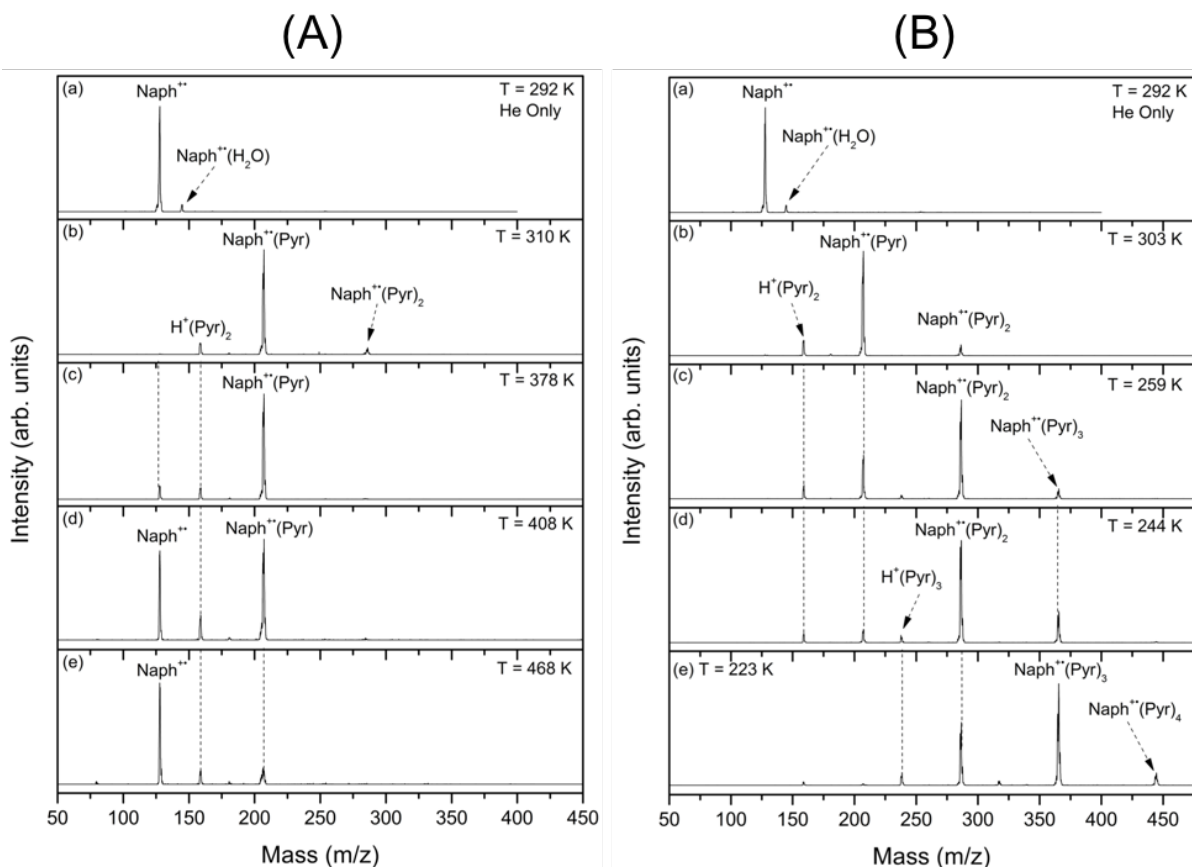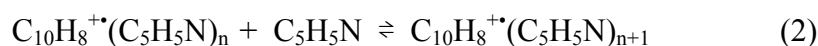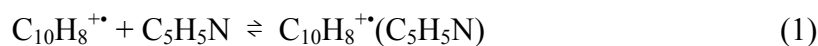**Figure 1(A).** Mass scans following the injection of naphthalene radical cation ($C_{10}H_8^{+\bullet}$, Naph$^{+\bullet}$) into He (a) or He/C_5H_5N (Pyr) gas mixture (b-e) in the drift cell at increasing temperatures shown. Total pressures (P_t) and pressure of C_5H_5N (P_{Pyr}) (Torr) inside the drift cell are: (a) P_t = 0.783; (b) P_t = 0.762, P_{Pyr} = 0.090; (c) P_t = 0.871, P_{Pyr} = 0.106; (d) P_t = 0.897, P_{Pyr} = 0.114; (e) P_t = 0.986, P_{Pyr} = 0.124.

Figure 1(B). Mass scans following the injection of naphthalene radical cation ($C_{10}H_8^{+\bullet}$, Naph$^{+\bullet}$) into He (a) or He/C_5H_5N (Pyr) gas mixture (b-e) in the drift cell at decreasing temperatures shown. Total pressures (P_t) and pressure of C_5H_5N (P_{Pyr}) (Torr) inside the drift cell are: (a) P_t = 0.783; (b) P_t = 0.810, P_{Pyr} = 0.098; (c) P_t = 0.768, P_{Pyr} = 0.096; (d) P_t = 0.765, P_{Pyr} = 0.093; (e) P_t = 0.772, P_{Pyr} = 0.046.

The observed association reactions of pyridine with the naphthalene radical cation are represented by equations (1) and (2):

$$C_{10}H_8^{+\bullet} + C_5H_5N \rightleftharpoons C_{10}H_8^{+\bullet}(C_5H_5N) \qquad (1)$$

$$C_{10}H_8^{+\bullet}(C_5H_5N)_n + C_5H_5N \rightleftharpoons C_{10}H_8^{+\bullet}(C_5H_5N)_{n+1} \qquad (2)$$

The equilibrium between Naph$^{+\bullet}$(Pyr)$_n$ and Naph$^{+\bullet}$(Pyr)$_{n+1}$ ions is verified by measuring intensity ratio $C_{10}H_8^{+\bullet}(C_5H_5N)_{n+1}/C_{10}H_8^{+\bullet}(C_5H_5N)_n$ from the integrated arrival ion distribution (ATD) peaks of $C_{10}H_8^{+\bullet}(C_5H_5N)_{n+1}$ and $C_{10}H_8^{+\bullet}(C_5H_5N)_n$ as a function of

8

decreasing the drift cell field corresponding to increasing reaction time, and equilibrium is achieved when a constant ratio is obtained.[52,53] Equilibrium is also verified by observing identical ATDs of the $C_{10}H_8^{+\bullet}(C_5H_5N)_n$ and $C_{10}H_8^{+\bullet}(C_5H_5N)_{n+1}$ ions since at equilibrium, the ATDs of the reactant and product ions must be identical.[52,53]

The equilibrium constants for reactions (1) and (2) with n = 0-3 measured at different temperatures yield the van't Hoff plots for the formation of the $C_{10}H_8^{+\bullet}(C_5H_5N)_{n+1}$ species with n+1 = 1-4 as shown in **Figure 2**. The measured equilibrium constants and van't Hoff plots are duplicated at least three times, and the estimated errors in ΔH^o and ΔS^o values are obtained from standard deviations of van't Hoff plots and from typical uncertainties in thermochemical equilibrium studies.[25,52,53] The resulting $-\Delta H^o$ and $-\Delta S^o$ values for the formation of $C_{10}H_8^{+\bullet}(C_5H_5N)_{n+1}$ for n+1 = 1-4 are given in **Table 1**.
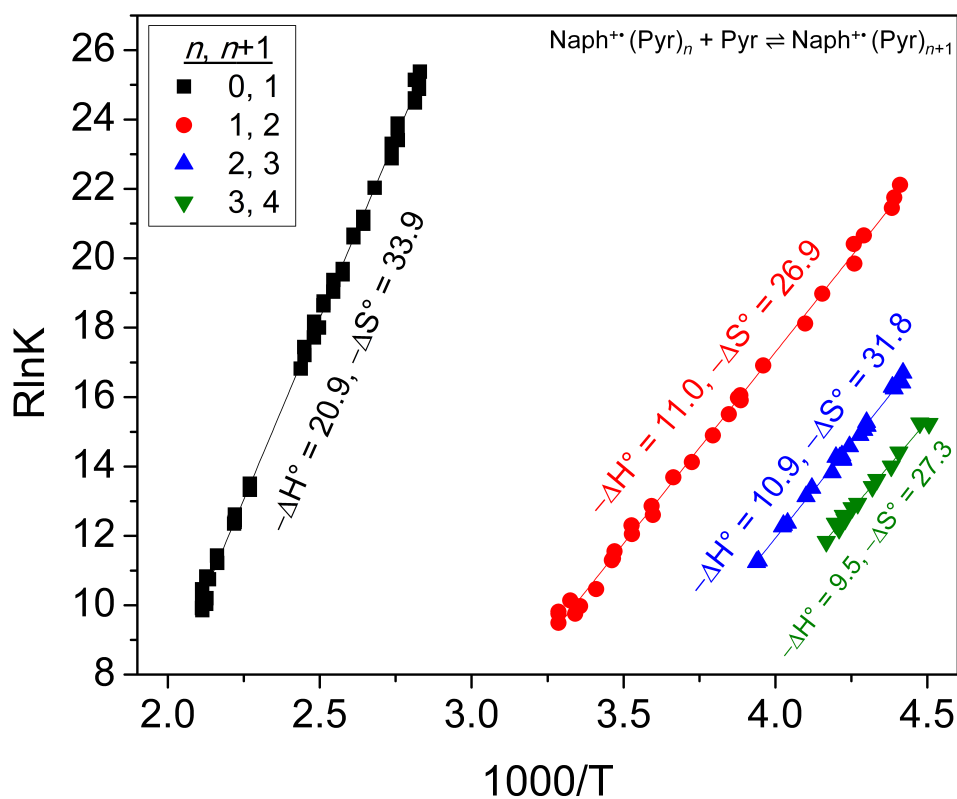

Figure 2. van't Hoff plots for the $C_{10}H_8^{+\bullet}(C_5H_5N)_n + C_5H_5N \rightleftarrows C_{10}H_8^{+\bullet}(C_5H_5N)_{n+1}$ reactions for *n* = 0-3.

Table 1. Thermochemistry for the step-wise addition of pyridine to the naphthalene radical cation.

$n, n+1$	$-\Delta H^{o}$ (kcal mol^{-1})	$-\Delta S^{o}$ (cal mol^{-1} K^{-1})
0, 1	20.9 ± 0.6	33.9 ± 1.1
1, 2	11.0 ± 0.5	26.9 ± 1.2
2, 3	10.9 ± 0.5	31.8 ± 1.3
3, 4	9.5 ± 0.8	27.3 ± 1.7

The measured enthalpy of binding of the Naph$^{+\bullet}$(Pyr) heterodimer (20.9 kcal/mol) is significantly larger than that of the Naph$^{+\bullet}$(Naph) homodimer (17.8 kcal/mol).[25] It is also significantly smaller than the binding of the Bz$^{+\bullet}$(Pyr) heterodimer (>33 kcal/mol).[13] The addition of the second pyridine molecule to the Naph$^{+\bullet}$(Pyr) heterodimer results in nearly 50% drop in the sequential binding enthalpy which appears to stay nearly constant at the 10-11 kcal/mol range with the subsequent addition of up to four pyridine molecules. This suggests that the nature of bonding in the Naph$^{+\bullet}$(Pyr) heterodimer is very different from clustering of pyridine molecules around the Naph$^{+\bullet}$(Pyr) heterodimer.

The stronger and more ordered structure of the Naph$^{+\bullet}$(Pyr) heterodimer is also evident by the large entropy loss resulting from the formation of the dimer (34 ± 1 cal mol^{-1} K^{-1}) which is larger than the corresponding $-\Delta S^{o}$ value for addition of the second pyridine molecule to the Naph$^{+\bullet}$(Pyr) adduct (27 ± 1 cal mol^{-1} K^{-1}). This may suggest that the formation of the Naph$^{+\bullet}$(Pyr) adduct results in a more ordered structure and highly directional interaction between the nitrogen lone pair of electrons of pyridine and the positively charged naphthalene radical cation. Although the third pyridine addition appears to involve higher negative entropy (32 ± 1 cal mol^{-1} K^{-1}), the limited number of data points and the general trend of increasing the uncertainties in the entropy values of higher equilibrium steps prevent accurate interpretation of this result.

To gain insight into the structure and the nature of the interaction in the Naph$^{+\bullet}$(Pyr) heterodimer and to understand the interesting changes in bond strengths compared to these related systems, it is essential to characterize the potential energy surface. For this purpose, we have carried out DFT calculations as discussed below.

Calculations of the Naphthalene$^{+\bullet}$(Pyridine) Structures

We identified three main classes of minima for the first encounter complex (FEC), as reported in Figure 3. The first class of minima is attributed to an almost parallel face-to-face

charge-transfer interaction similar to that in the naphthalene-benzene cation and is a very flat portion of the potential energy surface that sits about 8 kcal/mol below the reacting fragments (***f***-isomers). We identified at least six independent minima belonging to this class, differing only slightly in their geometry, and with energies and barriers all within 0.5 kcal/mol of each other. The second class of isomers is composed of isomers with a side-to-side interaction which form T-shaped complexes with an H-bond interaction between the two hydrogen in the α positions of the naphthalene cation and the nitrogen atom of pyridine (***h***-isomers). As for the previous class, this class is composed of at least four different minima with small differences due to the angle between the planes of the molecules, and all within 1 kcal/mol of each other and with very small interconversion barriers, and therefore we will report results for the lowest energy isomer, which sits about 12 kcal/mol below the reacting fragments. The third class of minima includes two distinct structures where a covalent bond is formed between the naphthalene and the pyridine fragments (***d***-isomers). The preference site for the bond formation follows the conventional reactivity of naphthalene for substitutions, with the isomer with the pyridine in α (***d1***) that sits about 35 kcal/mol below the reacting fragments and is more stable than the complex with the substituent in β (***d2***) by about 5 kcal/mol. Mulliken population analysis reveals that the positive charge in these structures is mostly delocalized between the three carbons located in the ortho- and para- position of the pyridine ring in both isomers, while the excess spin is delocalized mostly between two carbon atoms in the naphthalene ring.
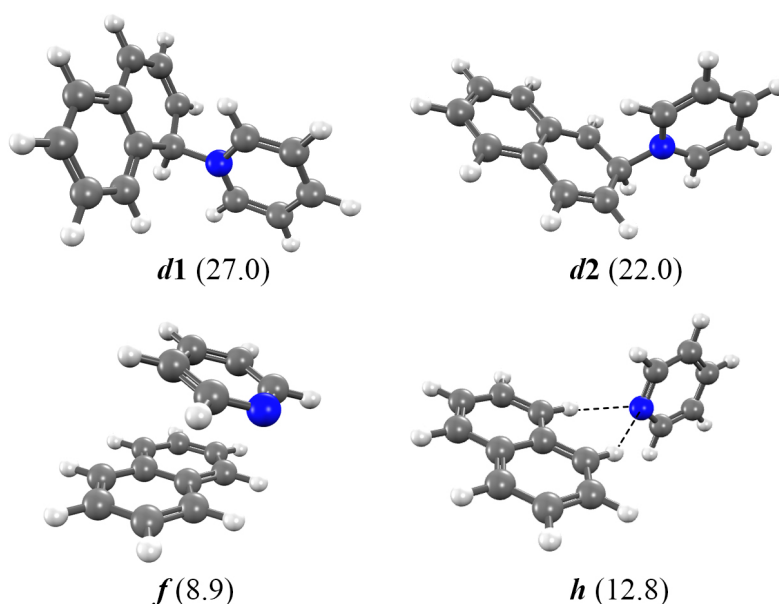

d1 (27.0)   ***d2*** (22.0)

f (8.9)   ***h*** (12.8)

Figure 3. First encounter complexes for the Naph$^{+\bullet}$(Pyr) system with the (calculated binding energies in kcal/mol).

The difference between measured and calculated binding energies can be explained by considering the possibility that an ensemble average of several minima is measured in the experiment, including *d*1, *d*2 and other isomers such as those that are derived from *d*1 and *d*2 via a migration of the proton at the reaction site to other locations in the naphthalene or in the pyridine rings. We calculated the thermodynamic correction using harmonic approximations for all possible isomers in the system and we collected the main results in **Table 2** (the full results are reported in the supporting information). The harmonic approximation is notoriously inappropriate for the calculation of the contribution to ΔS for weakly bonded minima (*f*- and *h*-isomers in this case), and therefore we estimated them using two different methods: *a*) by taking the experimental ΔS contribution from the similar naphthalene$^{+\bullet}$(benzene) system that we recently studied (averaging at -19.0 cal/mol K)[25], by using the harmonic oscillator results and considering the loss of translational degrees of freedom in favor of one vibration (averaging at -20.2 cal/mol K). Using either of these two estimated values has no effects on the final results of the Boltzmann averaging procedure, so we don't believe this to be a significant source of errors. The thermodynamic corrections ΔH[T] at the estimated experimental temperature of 400 K reduce the binding energy of all species by a significant amount, bringing the calculated binding enthalpy of *d*1 at 400 K down to 23.9 kcal/mol, a value that is closer to the experimental number. We also calculated the values of ΔG at 400 K, and the related composition of the Boltzmann average, and found that the ensemble contains at least seven minima with significant populations. 33% of the molecules in the ensemble are in the global minimum form *d*1, but of significant importance are also the minima *d*1.4 and *d*1.5 where the proton is transferred across the naphthalene ring. The barrier height for the *d*1/*d*1.4 conversion is calculated (including ZPE) at 20.4 kcal/mol over *d*1 (while the barrier for the *d*1.4/*d*1.5 should be of similar height), which suggests that this barrier can be overcome at the experimental conditions, and therefore the ensemble should be observed. A few other structures related to the *d*2 isomer are also involved in the ensemble, in particular *d*2.1, *d*2.5, *d*2.4 and *d*2.8, although their formation pathways might be more complex. It is interesting to note that *d*2 is not involved in the ensemble, as well as neither of the more weakly bound structures in the *h*-class and *f*-class. The Boltzmann analysis of the ensemble provides an average ΔH that is 23.4 kcal/mol, a value that is slightly higher than the experimental number (20.9 kcal/mol), but in substantial agreement.

Table 2. Electronic binding energies at 0K (kcal/mol), binding enthalpies and free energies at 400 K (kcal/mol), and Boltzmann composition (%) for significant isomers in the $Naph^{+\bullet}(Pyr)$ system. Full results are provided in the Supporting Information.

Isomer	$-\Delta E$	$-\Delta H$	$-\Delta G(400K)$	Boltzmann AVG Composition
*d*1	27.0	23.9	7.5	33
*d*2.1[a]	26.9	23.6	6.5	9
*d*1.4	26.4	23.5	6.6	11
*d*2.5	26.4	23.7	7.3	23
*d*1.5	25.6	22.8	6.6	10
*d*2.4	25.5	22.8	6.5	9
*d*2.8	25.3	22.5	5.9	4
*d*2	22.0	19.1	3.2	0
h	12.8	11.6	4.0	0
f	8.9	9.3	1.7	0

[a] The nomenclature used for the H-migrated isomers is determined from the parent first-encounter-complex (***d*1** with pyridine and hydrogen in position 1, or ***d*2** with pyridine and hydrogen in position 2), followed after the dot by the carbon to which the hydrogen has migrated, labelled using the standard convention illustrated to the right.
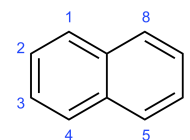
Collision Cross Section of the Naphthalene$^{+\bullet}$(Pyridine) Adduct

Ion mobility provides an accurate method for determining collision cross sections of mass-selected ions in a buffer gas.[29,30] The motion of the ion through a buffer gas under the influence of a weak electric field depends on the ion's average collision cross section (Ω, Å^2) with the buffer gas, which depends on the geometric shape of the ion.[11,29,30] Theoretical calculations of possible structural candidates of the mass-selected ions are then used to compute angle-averaged Ω's at different temperatures for comparison with the measured ones.[11,29,30]

To measure the mobility of the $Naph^{\bullet+}(Pyr)$ heterodimer, we generated the neutral dimer by a supersonic co-expansion of the naphthalene-pyridine vapor mixture in He followed by electron ionization. The mass spectrum following the injection of the ionized clusters into the drift cell containing helium at 310 K is shown in Figure 4-a. The peaks observed correspond to $Naph^{+\bullet}$, $(Pyr)_2^{+\bullet}$, $Naph^{+\bullet}(Pyr)$, and $Naph^{+\bullet}(Pyr)_2$. Mobility is determined according to Eq. 3, by plotting t_d versus P/V.

$$t_d = \left(\frac{l^2 \cdot 273.15}{T \cdot 760} \frac{1}{K_0} \right) \frac{P}{V} + t_0 \qquad (3)$$

Where t_d is the arrival time, K_0 is the reduced mobility (cm V^{-1} s^{-1}), P is the pressure in Torr and T is the temperature in Kelvin, l is the drift length (5 cm in our system), t_d is the measured mean arrival time of the drifting ion packet corrected for the non-Gaussian shape of the arrival time distribution (ATD) peak,[29,30] t_0 is the time the ion spends outside the drift cell before reaching the detector, and V is the voltage across the drift cell. All the mobility measurements were carried out in the low-field limit where the ion's drift velocity is small compared to the thermal velocity and the ion mobility is independent of the field strength (E/N < 5.0, where E is the electric field intensity and N is the gas number density and E/N is expressed in units of Townsend (Td) where 1 Td = 10^{-17} V. cm^2).[29,30] The ATDs and t_d versus P/V plots for the radical cations the naphthalene are displayed in Figures 4(b) and 4 (c), respectively. The slope of the linear plot is inversely proportional to the reduced mobility and the intercept equals the time spent within the second quadrupole before the detection of the ions.
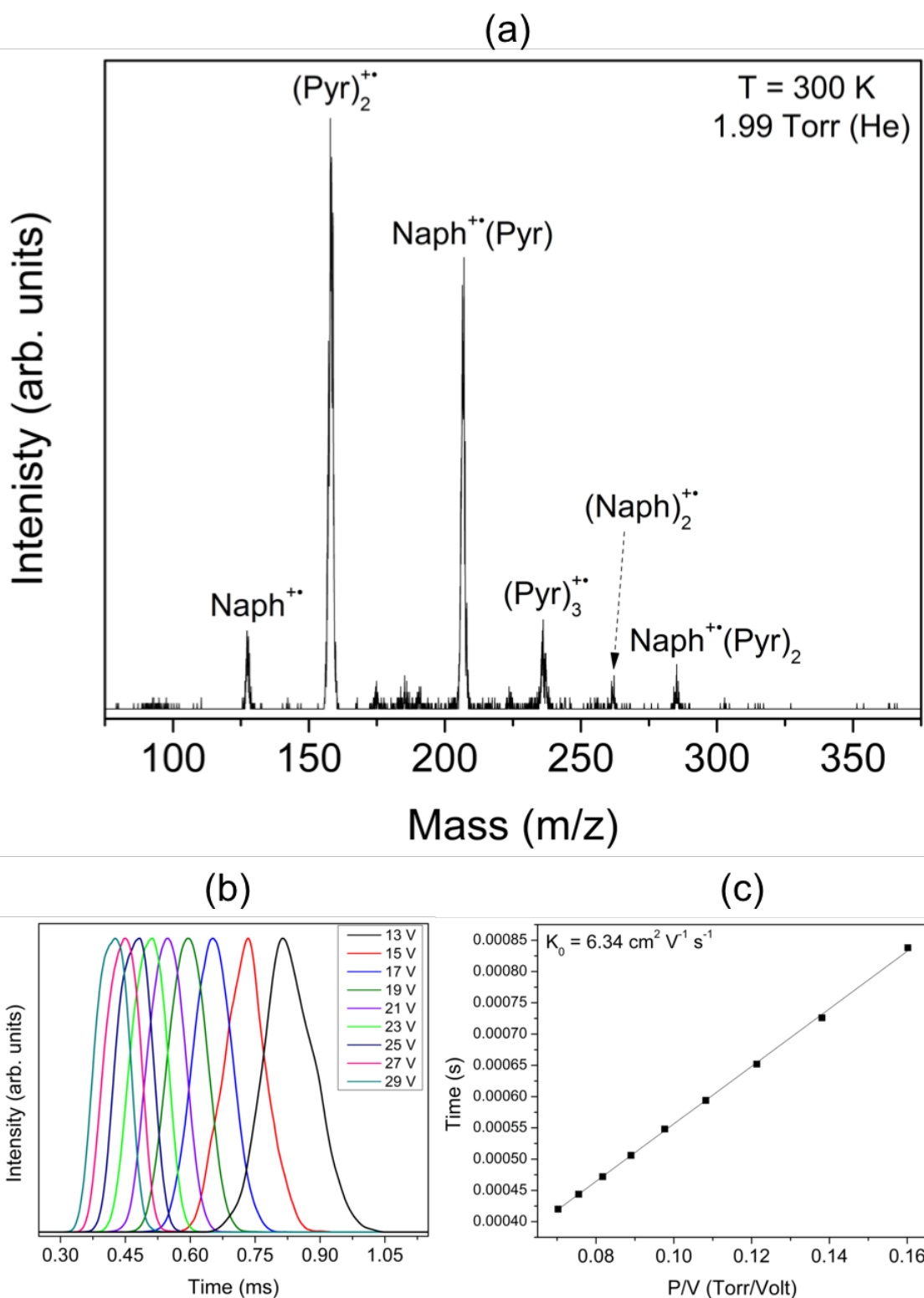
Figure 4. (a) Mass scans following the co-expansion of naphthalene ($C_{10}H_8$, Naph) and pyridine (C_5H_5, Pyr) into the drift cell containing He at the temperature and pressure shown. (b) ATDs and (c) t_d versus P/V plot for the Naph$^{+\bullet}$(Pyr) heterodimer. All data are obtained in 2.0 Torr helium at a temperature of 302 K.

According to the kinetic theory of gases, Eq. (4) relates the mobility of an ion to the average collision cross- section of the ion with the buffer gas.[29,30]

$$K = \frac{1}{N} \frac{(18 \cdot \pi)^{1/2}}{16} \left[\frac{1}{m} + \frac{1}{m_b} \right]^{1/2} \frac{z \cdot e}{(k_B \cdot T)^{1/2} \cdot \Omega^{(1,1)}{}_{avg}} \tag{4}$$

N is the buffer gas number density, m is the mass of the ion, m_b is the mass of a buffer gas atom, z is the number of charges, e is the electron charge, k_B is Boltzmann's constant and $\Omega^{(1,1)}{}_{avg}$ is the average collision integral. The measured mobilities at different temperatures are used to calculate average Ωs for the ion in helium using Eq. 4, and the resulting values are listed in **Table 3** as Ω_{exp} (Å^2) for the Naph$^{+\bullet}$(Pyr) heterodimer. The collision cross section of the Naph$^{+\bullet}$(Pyr) dimer is 84.9±2.5 Å^2 at 302 K and increases slightly to 87.5±2.3 Å^2 at 223 K. Angle-averaged collision cross-sections are computed at different temperatures for the four isomers calculated at the M06-2X/cc-pVTZ level of theory using the trajectory method.[54] The theoretical Ω's are then compared to the experimentally measured values to identify the most likely structures as summarized in **Table 3**.

Table 3. Experimental-based collision cross sections of the Naph$^{+\bullet}$(Pyr) heterodimer in helium at different temperatures as indicated. The calculated cross sections obtained from the trajectory method for two covalent (**d1** and **d2**), stacked parallel, and T-shaped structures optimized at M06-2X/cc-pVTZ level of theory. The bold face values represent the best agreement between the experimental and calculated cross sections.

Temp (K)	K_0 (cm V^{-1} s^{-1})	Ω (Å^2) Exp.	Ω (Å^2) Calc. (**d1**)	Ω (Å^2) Calc. (**d2**)	Ω (Å^2) Calc. Stacked Parallel (**f**)	Ω (Å^2) Calc. T-Shaped (**h**)
302	6.32	**84.9 ± 2.5**	**83.9**	**85.1**	79.8	92.0
273	6.53	**86.5 ± 2.5**	**85.3**	**86.5**	81.1	93.4
223	7.18	**87.5 ± 2.3**	**88.4**	**89.6**	84.2	96.6

The measured collision cross sections for the Naph$^{+\bullet}$(Pyr) heterodimer at 302 K and 273 K are in good agreement with the calculated values of the covalent structures **d1** and **d2**. At 302 and 273 K, the measured collision cross sections, 84.9±2.5 and 86.5±2.5 Å^2, are close to the calculated values, 83.9 and 85.3 Å^2 for the **d1** structure and 85.1 and 86.5 Å^2 for the **d2** structure, respectively. At 223 K, the measured collision cross section is 87.5±2.3 Å^2, which is very close to the calculated cross sections of 88.4 and 89.6 Å^2 for the **d1** and **d2** structures, respectively. For the stacked parallel structure (**f**), the calculated collision cross sections are

79.8, 81.1, and 82.4 Å^2 at 302, 273, and 223 K respectively. At all temperatures, the calculated cross sections for the stacked parallel structure are significantly smaller than the measured collision cross sections. Alternatively, the calculated collision cross sections for the T-shaped h isomer (92.0, 93.4, and 96.6 Å^2 at 302, 273, and 223 K, respectively), are about 10% larger on average than the measured collision cross sections. Based on these comparisons, a mixture of covalent distonic structures based on $d1$ and $d2$ is likely to be present under the experimental conditions. This is consistent with the computational predictions discussed in the previous section.

Comparison with the Benzene$^{+•}$(Pyridine) and Benzene$^{+•}$(Ammonia) σ-Complexes

It is interesting to compare the binding energy of the newly formed C–N σ bond in $d1$ to the similar bond in the Bz$^{+•}$(Pyr) complex.[13] In particular, the C–N bond in the distonic structure of Bz$^{+•}$(Pyr) is calculated to be a striking 16 kcal/mol more stable than the analogous structure for Naph$^{+•}$(Pyr). This is surprising considering that the C-N bond lengths are identical (1.54 Å in Bz$^{+•}$(Pyr) vs 1.54 Å in Naph$^{+•}$(Pyr)), and so no correlation between bond strength and bond length is operative. Our new calculations, in fact, suggest that the distonic structure of Bz$^{+•}$(Pyr) has a higher binding energy of 42.3 kcal/mol (ωB97X-V/pc3), than previously thought (our previously published result of 26.4 kcal/mol was obtained with substantially lower-level B3LYP/6-311G(d,p) calculations). What is the origin of the significant difference between binding energies?

To unravel this puzzle, we also performed calculations on other distonic complexes involving benzene and naphthalene. It turns out to be instructive to also consider benzene$^{+•}$(ammonia),[26-28] and naphthalene$^{+•}$(ammonia) complexes, which are shown in **Figure 5**. These ammonia complexes have binding energies which differ by 14 kcal/mol, with the benzene complex again more stable. ALMO-EDA[41,42] was used to decompose the total binding energy into the geometric-distortion (GD), frozen interaction (FRZ), polarization (POL), and charge-transfer (CT) components, as shown in **Table 4**. We will examine these components to see whether we can obtain insight into the origin of the difference between benzene and naphthalene (benzene complex much more stable), as well as between ammonia and pyridine (pyridine complex much more stable).
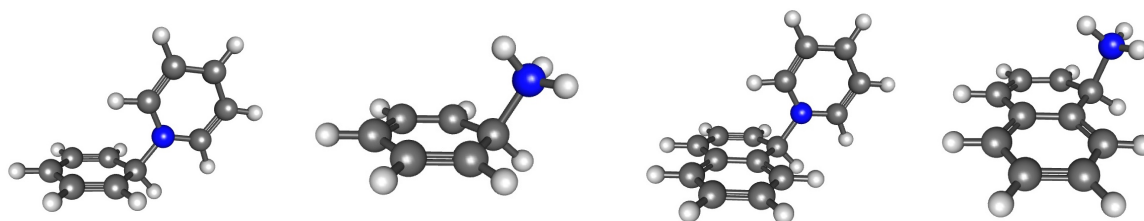
Figure 5. Structures of the four complexes with covalent C–N σ bonds. From left to right, benzene[+•](pyridine),[13] benzene[+•](ammonia),[26-28] the **d1** isomer of naphthalene[+•](pyridine) and the naphthalene[+•](ammonia), respectively.

Table 4. Energy decomposition analysis (kcal/mol) results for the four complexes with covalent C–N σ bond.

	Benzene[+•](pyridine)	Naphthalene[+•](pyridine)	Benzene[+•](ammonia)	Naphthalene[+•](ammonia)
GD	23.7	29.0	19.4	22.6
FRZ	153.6	170.0	139.4	156.0
Elec.	-76.8	-79.5	-69.5	-71.1
Pauli	247.5	267.8	222.2	240.8
Disp.	-17.1	-18.3	-13.3	-13.7
POL	-128.9	-136.3	-91.1	-98.6
CT	-90.7	-89.0	-94.0	-92.1
TOT	-42.3	-26.3	-26.3	-12.2

From the EDA, the major difference between the naphthalene and benzene case appears to be in the frozen interaction term. Further separation of this term[42] into electronic (Elec), Pauli repulsion, and dispersion (Disp) contributions reveals that the lower binding energy of the naphthalene system is due to the Pauli repulsion term, which is about 20 kcal/mol more repulsive than for the benzene case. Geometric distortion also contributes a further 5 kcal/mol, while dispersion and charge-transfer are essentially very similar. The attractive polarization term stabilizes the more polarizable naphthalene by a substantial 8 kcal/mol more than the benzene complex, but the overall interaction energy still remains about 16 kcal/mol higher for the benzene complex. Evidently bad contacts in the formation of the dative CN bond (this character is evident from the fact that CT itself exceeds the bond energy) are unavoidably greater with naphthalene than benzene.

The most likely reason for this difference is the greater delocalization of the positive charge in the isolated naphthalene cation relative to benzene cation, which will lead to

slightly less orbital contraction (in the frozen wavefunction) at the site attacked by the nitrogen lone pair. Subsequent electronic reorganization to localize the positive charge then leads to greater energy lowering from polarization in naphthalene complexes. Finally, with the charge localized, the energy lowering due to charge transfer from the nitrogen lone pair looks similar in both complexes. Strong support for this conclusion comes from the very similar differences in the benzene and naphthalene cation complexes with ammonia.

The origin of the stability difference between the ammonia and pyridine complexes is the net result of two principal factors. The fact that pyridine is a bulkier ligand than ammonia means that Pauli repulsion is inevitably stronger in its complexes (by about 15 kcal/mol), an effect that is not nearly compensated for by a slightly more favorable dispersion interaction. However, the Pauli penalty is more than compensated by the fact that pyridine is much more polarizable than ammonia, and the polarization energy lowering strongly favors (by about 28 kcal/mol) the pyridine coordination versus ammonia coordination in the radical cation complexes with either benzene or naphthalene.

The strengths (both absolute and relative) of the dative bonds in the four C-N complexes shown in **Figure 5** are controlled by factors that reflect the competition between driving forces for stability (polarization, charge transfer, electrostatics, and dispersion), and causes of electronic frustration (Pauli repulsion and geometric distortion, which captures loss of aromaticity due to rehybridization). Despite being more polarizable, the naphthalene complexes are destabilized relative to benzene by Pauli repulsion. On the other hand, far greater difference in polarizability of pyridine relative to ammonia makes its complexes more stable, despite the inevitably greater Pauli repulsion.

Reaction Reversibility of Benzene$^{+\bullet}$(Pyridine) vs. Naphthalene$^{+\bullet}$(Pyridine)

In order to explain the reversibility of the reaction to form the Naph$^{+\bullet}$(Pyr) complex and to compare to the Bz$^{+\bullet}$(Pyr) case, we analyzed the potential energy surface by searching for transition barriers using the freezing string method.[55] We looked for the H-migration barriers within the *d*-isomers (also including the barriers between *d*1 and *d*2, between the *f* and *d* isomers, and between the *h* and *d* isomers). Our results, summarized in **Figure 6**, show that the barriers for the proton migrations within the *d*-isomers are usually between 10 and 20 kcal/mol, while the barriers between the other minima are all very small. The covalently bound structure *d*1 is the global minimum for the Naph$^{+\bullet}$(Pyr) system, while the analogous structure is not the global minimum for Bz$^{+\bullet}$(Pyr). The minimum for the Bz$^{+\bullet}$(Pyr) system is a migration isomer that forms via a two-step reaction that passes through the FEC with *d*1-like

structure which undergoes subsequent proton migration from the benzene to the pyridine ring. We calculated the barrier of this reaction at about 30 kcal/mol over the first-encounter-complex. According to the experimental binding energy, the system has sufficient initial energy to find a way to overcome the first barrier and to form the migration isomer, but the half-life for reforming the first-encounter-complex at 400 K is larger than 3800 seconds, a time that is not compatible with the experimental conditions, therefore explaining why the reaction is observed to proceed irreversibly. The situation with the Naph[+•](Pyr) system is obviously more complex, with a number of different minima involved. The calculated barriers all have a half-life compatible with the experimental conditions (e.g., the half-life for reforming d1 from d1.4 is only 0.7 ms). This explains why the rearrangements are reversible, and supports the hypothesis that several minima are accessible at the experimental conditions.
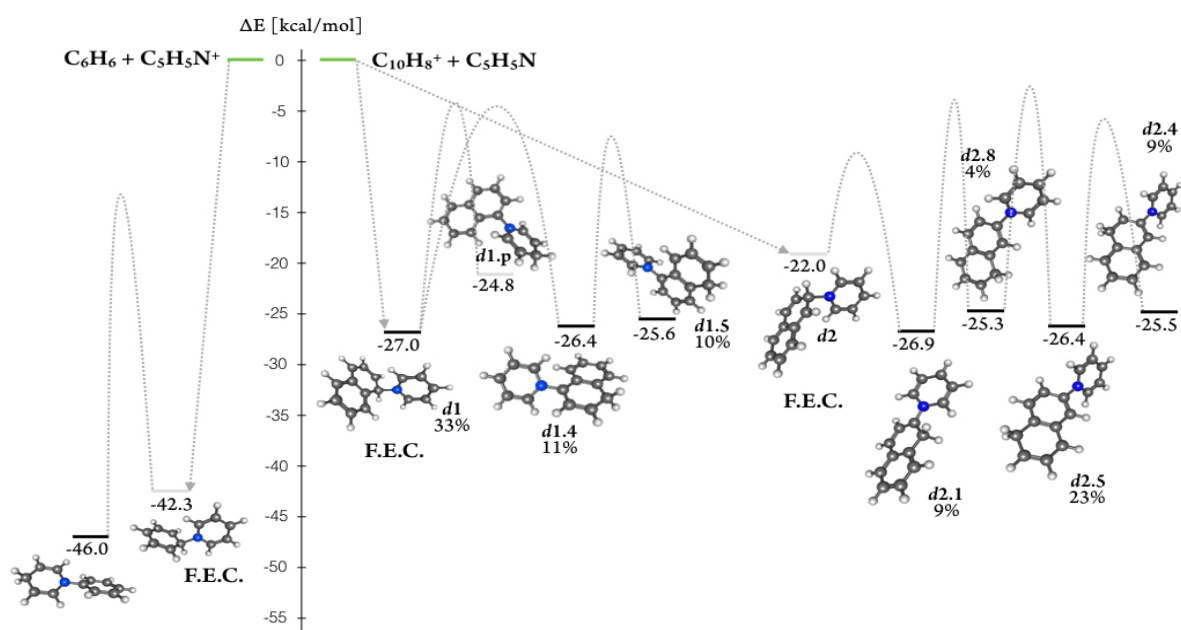

Figure 6. Reaction diagrams for the formation of the naphthalene[+•](pyridine) adduct (the percentage population of key isomers in the 400 K ensemble is also indicated) as compared to the (benzene.pyridine)[+•] adduct (left to the energy scale).

Addition of Further Pyridine Molecules

The addition of a second pyridine molecule to the Naph[+•](Pyr) complex does not result in the formation of a new covalent bond. Our AIMD and QAIMD simulations show that the second pyridine molecule arranges in a way that forms a network of hydrogen bonds

among the three molecules involved in the complex. Starting from the two lowest energy isomers identified in the previous section, $d1$ and $d2$, we obtain the four lowest-energy isomers reported in **Figure 7**, with the extra pyridine molecule on either the same side (SS) or the opposite side (OS) of the naphthalene ring where the first pyridine is attached. By starting from other isomers of the heterodimer, we obtain a plethora of minima where the second pyridine always arranges to form a hydrogen bond network in the complex, such as for the lowest energy isomers in **Figure 7**. Despite the number of structures in $Naph^{+\bullet}(Pyr)_2$ being much higher than in $Naph^{+\bullet}(Pyr)$, the second pyridine interacts with the dimer always in the same way, resulting in a small range for the calculated binding energy of the second pyridine, calculated at 12 to 13 kcal/mol. Including thermal corrections, the calculated $-\Delta H^o$ is 12 ± 1 kcal/mol, a value that is in very good agreement with the measured value of 11.2 kcal/mol. From the chemical bonding standpoint, we infer that the incremental charge-transfer stabilization associated with covalent linking of a second pyridine molecule to the $Naph^{+\bullet}(Pyr)$ is insufficient to compensate further loss of aromaticity and Pauli repulsion.
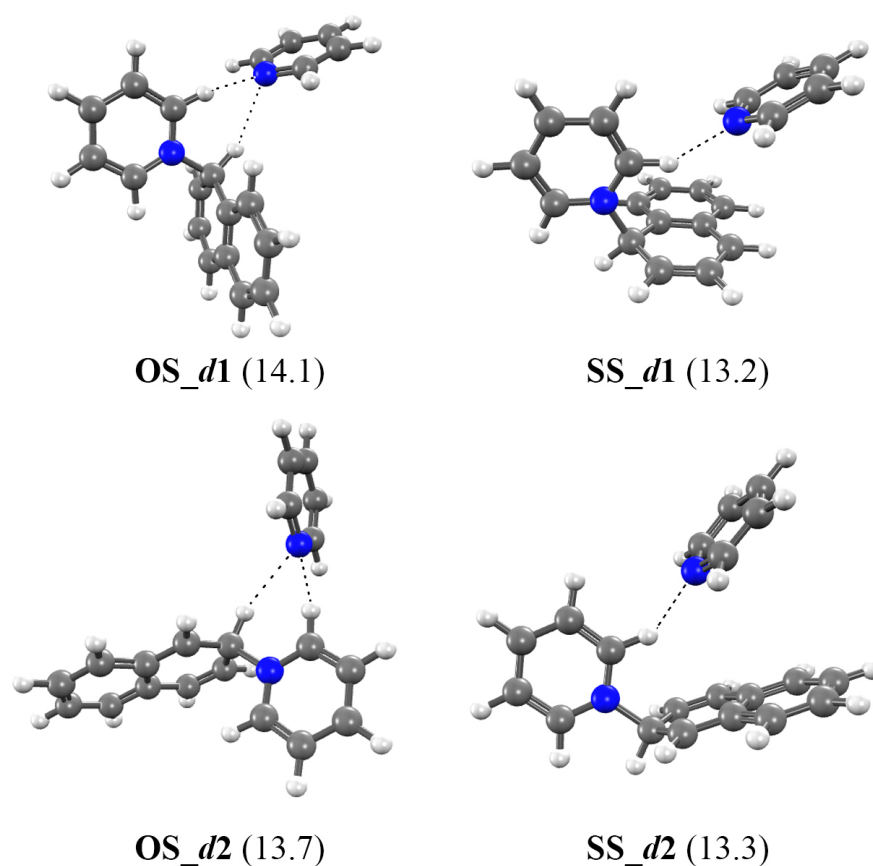

OS_$d1$ (14.1)   **SS_$d1$** (13.2)

OS_$d2$ (13.7)   **SS_$d2$** (13.3)

Figure 7. Lowest-energy isomers for the $Naph^{+\bullet}(Pyr)_2$ complex with (calculated binding energies in kcal/mol).

We also performed a limited investigation (because of the enormous size of the potential energy surface) of the addition of the third and fourth pyridine molecules to the complex. The Naph$^{+\bullet}$(Pyr)$_3$ system shows results that are in line with those for Naph$^{+\bullet}$(Pyr)$_2$. Again, no formation of new covalent bonds is observed, and the third pyridine molecule arranges on the same side of the naphthalene ring where the other two pyridine fragments are, in a pattern that maximizes the number of hydrogen bond interactions between the N terminal of the pyridine and different hydrogen atoms in the system. We identified more than ten minima with diverse structures and hydrogen bond patterns, but with energies that differ by less than 0.1 kcal/mol between each other, resulting in binding energies of roughly 11–13 kcal/mol for each structure. The potential energy surface for the addition of the fourth pyridine is obviously even flatter, and the yet larger size of the system makes it computationally challenging to explore. From our limited number of completed calculations, the fourth pyridine attaches to the complex through hydrogen-bond interactions, but the preferred side is the empty side of the naphthalene ring. For this reason, the binding energy for this fourth addition is calculated as slightly smaller (~8 kcal/mol). These results are also in substantial agreement with the experiments, for which additions are observed for up to four pyridine molecules, with binding energies that are similar for the second and third addition, and slightly lower for the fourth addition. According to very limited pilot calculations on the potential energy surfaces of the tetramer and pentamer, a fifth pyridine addition should be possible on the less crowded side of the naphthalene, with a calculated binding energy of about 4–7 kcal/mol.

CONCLUSIONS

Association between radical cations and neutrals gives a wide range of bonding motifs and interaction strengths, due to the rich interplay of attraction associated with permanent and induced electrostatics and charge transfer, versus repulsions due to Pauli repulsions and structural deformations. In this work we have explored experimentally and computationally how these factors play out in the complexes formed from the interaction of the radical cation of naphthalene with pyridine molecules.

The thermodynamics of association of naphthalene$^{+\bullet}$(pyridine) were characterized experimentally, showing $\Delta H^o = -20.9 \pm 0.6$ kcal/mol (at 400 K) and $\Delta S^o = -33.9 \pm 1.1$ cal mol^{-1} K^{-1}. The enthalpy change is significantly smaller than the lower limit (<-33 kcal/mol) reported previously for formation of the radical cation complex between benzene and pyridine, (benzene.pyridine)$^{+\bullet}$. The entropy change is far more negative than the

naphthalene[++•](benzene) complex recently reported between the naphthalene radical cation and benzene (-19 kcal mol^{-1} K^{-1}), suggesting a significantly more ordered structure in naphthalene[++•](pyridine).

The origin of these results was explored using electronic structure calculations. The global minimum on the radical complex PES is the distonic complex *d*1 (see Figure 3) formed by pyridine attack on naphthalene radical cation at the α-carbon position, resulting in a hybridization change from sp^2 to distorted sp^3 at that position. Indeed this is much more ordered structure than the stacking complex calculated to be the preferred form of the naphthalene[++•](benzene) complex. A rich array of isomers of slightly higher energies arises from proton hops to different sites, as well as corresponding derivatives of the analogous *d*2 isomer. Boltzmann averaging suggests that a mixture of isomers is present at the temperatures considered experimentally. Experimental collision cross-sections obtained from ion mobility measurements are consistent with this interpretation.

A calculated 16 kcal/mol reduction in the binding energy of naphthalene[++•](pyridine) relative to (benzene.pyridine)[++•] was rationalized using energy decomposition analysis (EDA), which showed that Pauli repulsion is intrinsically higher for the naphthalene complex, despite more favorable polarization. This interpretation was supported by additional calculations showing a very similar reduction in enthalpy of association in naphthalene[++•](NH_3) relative to benzene[++•](NH_3), with analogous changes in EDA terms. The EDA showed conclusively that the driving force for complex formation is charge-transfer (CT). Finally, the ammonia complexes are weaker than the corresponding pyridine complexes because the polarizability enhancement in pyridine more than compensates additional Pauli repulsion, while the CT driving force is similar.

ASSOCIATED CONTENT

Supporting Information

AUTHOR INFORMATION

Corresponding Authors

M. Samy El Shall (mselshal@vcu.edu) and Martin Head-Gordon (mhg@cchem.berkeley.edu)

Notes

The authors declare no competing financial interests.

References

1. Frenklach, M. Reaction Mechanism of Soot Formation in Flames, *Phys. Chem. Chem. Phys*. **2002**, 4, 2028-2037.

2. Homann, K-H. Fullerenes and Soot Formation—New Pathways to Large Particles in Flames, *Angew. Chem. Inter. Ed,* **1998**, 37, 2434–2451.

3. Herbst, E.; van Dishoeck, E. F. Complex Organic Interstellar Molecules, *Annual Rev. Astronomy and Astrophysics* **2009**, 47, 427-480.

4. Tielens, A. G. G. M., "Interstellar Polycyclic Aromatic Hydrocarbon Molecules", *Ann. Rev. Astron. Astrophys.* **2008**, 46, 289–337.

5. Rhee, Y. M.; Lee, T. J.; Gudipati, M. S.; Allamandola, L. J. and Head-Gordon, M. "Charged Polycyclic Aromatic Hydrocarbon Clusters and the Galactic Extended Red Emission", *Proceedings of the National Academy of Sciences USA* **2007**, 104, 5274-5278.

6. Lopez-Puretas, M.; Dinello, B. M.; Adriani, A.; Funke, B.; Garcia-Comas, M.; Mpricono, M. L.; D'Aversa, E.; Boersma, C.; Allamandola, L. J. "Large Abundances of Polycyclic Aromatic Hydrocarbons in Titan's Upper Atmosphere", *Astrophys. J.* **2013**, 770, 132.

7. Nuth, J. A.; Kimura, Y.; Lucas, C.; Ferguson, F.; Johnson, N. M. The Formation of Graphite Whiskers in the Primitive Solar Nebula, *The Astrophysical Journal Letters.* **2010**, 710 L98.

8. Cable, M. L.; Hoerst, S. M.; Hodyss, R.; Beauchamp, P. M.; Smoth, M. A.; Willis, P. A. "Titan's Tholins: Simulating Titan Organic Chemistry in the Cassini-Huygens Era", *Chem. Rev.* **2011**, 112, 1882,

9. Steglich, M.; Bouwman, J.; Huisken, F.; Henning, Th. "Can Neutral and Ionized Polycyclic Aromatic Hydrocarbons be Carriers of the Ultraviolet Extinction Bump and the Diffuse Interstellar Bands?", *Astrophys. J.* **2011**, 742, 2

10. Berne, O.; Tielens, A. G. G. M. "Formation of Buckminsterfullerence (C_{60}) in Interstellar Space", *Proceedings of the National Academy of Sciences USA* **2012**, 109, 401-406.

11. Momoh, P. O.; Abrash, S. A.; Mabourki, R. and El-Shall, M. S. Polymerization of Ionized Acetylene Clusters into Covalent Bonded Ions. Evidence for the Formation of Benzene Radical Cation, *J. Am. Chem. Soc*. **2006**, 128, 12408-12409.

12. Snow, T. P.; Bierbaum, V. M. Ion Chemistry in the Interstellar Medium, *Annul. Rev. Anal. Chem.* **2008**, *1*, 229.

13. El-Shall, M. S.; Ibrahim, Y. N.; Alsharaeh, E. H.; Meot-Ner (Mautner), M.; Watson, S. P. Reactions between Aromatic Hydrocarbons and Heterocycles: Covalent and Proton-bonded Dimer Ions of Benzene/Pyridine, *J. Am. Chem. Soc*. **2009**, 131, 10066-10076.

14. Ascenzi, D.; Aysina, J.; Tosi, P.; Maranza, A.; Tonachini, G. Growth of Polyaromatic Molecules via Ion-Molecule Reactions: An Experimental and Theoretical Mechanistic Study, *J. Chem. Phys*. **2010**, 133, 184308.

15. Momoh, P. O.; Hamid, A. M.; Abrash, S. A.; El-Shall, M. S. Structure and Hydration of the $C_4H_4^{\bullet+}$ Ion formed by Electron Impact Ionization of Acetylene Clusters, *J. Chem. Phys*. **2011**, 134, 204315.

16. Soliman, A. R.; Hamid; A. M.; Momoh; P. O.; El-Shall, M. S.; Taylor; D.; Gallagher; L.; Abrash, S. A. Formation of Complex Organics in the Gas Phase by Sequential Reactions of Acetylene with the Phenylium Ion, *J. Phys. Chem. A* **2012**, 116, 8925–8933.

17. Soliman, A. R.; Hamid, A. H.; Attah, I.; Momoh, P.; El-Shall, M. S. Formation of Nitrogen-Containing Polycyclic Cations by Gas-Phase and Intracluster Reactions of Acetylene with the Pyridinium and Pyrimidinium Ions, *J. Am. Chem. Soc*. **2013**, 135, 155-166.

18. Hamid, A. M.; Bera, P. P.; Lee, T. J.; Aziz, S. G.; Al-Youbi, A. O.; El-Shall, M. S. Evidence for the Formation of Pyrimidine Cations from the Sequential Reactions of Hydrogen Cyanide with the Acetylene Radical Cation, *J. Phys. Chem. Lett.* **2014**, 5, 3392-3398.

19. Momoh, P.O.; Attah, I. K.; El-Shall, M. S.; Kanters, R. P. F.; Pinski, J. M.; Abrash, S. A. Formation of Covalently Bonded Polycyclic Hydrocarbon Ions by Intracluster Polymerization of Ionized Ethynylbenzene Clusters, *J. Phys. Chem. A* **2014**, 118, 8251-8263.

20. Soliman, A. R.; Attah, I. K.; Hamid, A. M.; El-Shall, M. S. Growth Kinetics and Formation Mechanisms of Complex Organics by Sequential Reactions of Acetylene with Ionized Aromatics, *Inter. J. Mass Spectrom* **2015**, 377, 139-151.

21. Attah, I. K.; Soliman, A. R.; Platt, S.; Meot-Ner, M.; Aziz, S.;.El-Shall, M. S. Observation of Covalent and Electrostatic Bonds in Nitrogen-Containing Polycyclic Ions Formed by Gas Phase Reactions of the Benzene Radical Cation with Pyrimidine, *Phys. Chem. Chem. Phys*. **2017**, 19, 6422-6432.

22. Meot-Ner (Mautner), M. Dimer Cations of Polycyclic Aromatics. Experimental Bonding Energies and Resonance Stabilization, *J. Phys. Chem*. **1980**, 84, 2724-2728.

23. Meot-Ner (Mautner), M.; El-Shall, M. S. Ionic Charge Transfer Complexes. 1. Cationic Complexes with Delocalized and Partially Localized π Systems, *J. Am. Chem. Soc*. **1986**, 108, 4386-4390.

24. El-Shall, M. S.; Meot-Ner (Mautner), M. Ionic Charge Transfer Complexes. 3. Delocalized π-Systems as Electron Acceptors and Donors. Dimer Cations of Naphthalene Derivatives, *J. Phys. Chem.***1987**, 91, 1088-1095.

25. Attah, I. K.; Platt, S. P.; Meot-Ner Mautner, M.; El-Shall, M. S.; Peverati, R.; Head-Gordon, M. What is the Structure of the Naphthalene–Benzene Heterodimer Radical Cation? Binding Energy, Charge Delocalization, and Unexpected Charge-Transfer Interaction in Stacked Dimer and Trimer Radical Cations, *J. Phys. Chem. Lett*. **2015**, 6, 1111–1118.

26. Tachikawa, H. An Ab-Initio Direct Trajectory Study on the Ionization Processes of the Benzene–NH3 complexes: Electronic State Dependence on the Complex Formation Processes, *Phys. Chem. Chem. Phys*. **2002**, 4, 6018–6026.

27. Mizuse, K.; Fujii, A.; Mikami, N. Infrared and Electronic Spectroscopy of a Model System for the Nucleophilic Substitution Intermediate in the Gas Phase: the C−N Valence Bond Formation in the Benzene−Ammonia Cluster Cation, *J. Phys. Chem. A* **2006**, 110, 6387–6390.

28. Mizuse, K.; Hasegawa, H.; Mikami, N.; Fujii, A. Infrared and Electronic Spectroscopy of Benzene−Ammonia Cluster Radical Cations $[C_6H_6(NH_3)_{1,2}]^+$: Observation of Isolated and Microsolvated Σ-Complexes. *J. Phys. Chem. A* **2010**, 114, 11060–11069.

29. Rusyniak, M.; Ibrahim, Y.; Wright, D.; Khanna, S. and El-Shall, M. S. Gas Phase Ion Mobilities and Structures of Benzene Cluster Cations $(C_6H_6)_n^+$, n = 2-6., *J. Am. Chem. Soc.* **2003**, 125, 12001-12013.

30. Platt, S. P.; Attah, I. K.; Aziz, S.; El-Shall, M. S. Ion Mobility of the Radical Cation Dimers: $(Naphthalene)_2^{+.}$ And $Naphthalene^+(Benzene)$: Evidence for Stacked Sandwich and T-shape Structures, *J. Chem. Phys.* **2015**, 142, 19112.

31. Mardirossian, N.; Head-Gordon, M. ωB97X-v: a 10-Parameter, Range-Separated Hybrid, Generalized Gradient Approximation Density Functional with Nonlocal Correlation, Designed by a Survival-of-the-Fittest Strategy, *Phys. Chem. Chem. Phys.* **2014**, 16, 9904–9924.

32. Dunning, T. H. Gaussian-Basis Sets for Use in Correlated Molecular Calculations. 1. the Atoms Boron Through Neon and Hydrogen. *J. Chem. Phys.* **1989**, 90, 1007–1023.

33. Becke, A. D. Density-Functional Exchange-Energy Approximation with Correct Asymptotic-Behavior. *Phys. Rev. A* **1988**, 38, 3098–3100.

34. Lee, C.; Yang, W.; Parr, R. G. Development of the Colle-Salvetti Correlation-Energy Formula into a Functional of the Electron-Density. *Phys. Rev. B* **1988**, 37, 785–789.

35. Stephens, P.; Devlin, F.; Chabalowski, C.; Frisch, M. J. Ab-Initio Calculation of Vibrational Absorption and Circular-Dichroism Spectra Using Density-Functional Force-Fields. *J. Phys. Chem.* **1994**, 98, 11623–11627.

36. Zhao, Y.; Truhlar, D. G. A New Local Density Functional for Main-Group Thermochemistry, Transition Metal Bonding, Thermochemical Kinetics, and Noncovalent Interactions. *J. Chem. Phys.* **2006**, 125, 194101.

37. Peverati, R.; Truhlar, D. G. Improving the Accuracy of Hybrid Meta-GGA Density Functionals by Range Separation. *J. Phys. Chem. Lett.* **2011**, 2, 2810–2817.

38. Moller, C.; Plesset, M. Note on an Approximation Treatment for Many-Electron Systems. *Phys.Rev.* **1933**, 46, 0618–0622.

39. Gerenkamp, M.; Grimme, S. Spin-Component Scaled Second-Order Møller–Plesset Perturbation Theory for the Calculation of Molecular Geometries and Harmonic Vibrational Frequencies. *Chem. Phys. Lett.* **2004**, 392, 229–235.

40. Lochan, R. C.; Head-Gordon, M. Orbital-Optimized Opposite-Spin Scaled Second-Order Correlation: an Economical Method to Improve the Description of Open-Shell Molecules. *J. Chem. Phys.* **2007**, 126, 164101.

41. Horn, P. R.; Head-Gordon, M. Polarization Contributions to Intermolecular Interactions Revisited with Fragment Electric-Field Response Functions. *J. Chem. Phys.* **2015**, 143, 114111.

42. Horn, P. R.; Mao, Y.; Head-Gordon, M. Probing Non-Covalent Interactions With a Second Generation Energy Decomposition Analysis Using Absolutely Localized Molecular Orbitals, *Phys. Chem. Chem. Phys.* **2016**, 18, 23067-23079.

43. Khaliullin, R. Z.; Head-Gordon, M.; Bell, A. T. An efficient Self-Consistent Field Method for Large Systems of Weakly Interacting Components. *J. Chem. Phys.* **2006**, 124, 204105–204112.
44. Khaliullin, R. Z.; Cobar, E. A.; Lochan, R. C.; Bell, A. T.; Head-Gordon, M. Unraveling the Origin of Intermolecular Interactions Using Absolutely Localized Molecular Orbitals. *J. Phys. Chem. A* **2007**, 111, 8753–8765.

45. Khaliullin, R. Z.; Bell, A. T.; Head-Gordon, M. Analysis of Charge Transfer Effects in Molecular Complexes Based on Absolutely Localized Molecular Orbitals. *J. Chem. Phys.* **2008**, 128, 184112.

46. Horn, P. R.; Sundstrom, E. J.; Baker, T. A.; Head-Gordon, M. Unrestricted Absolutely Localized Molecular Orbitals for Energy Decomposition Analysis: Theory and Applications to Intermolecular Interactions Involving Radicals. *J. Chem. Phys.* **2013**, 138, 134119.

47. Jensen, F.; Polarization Consistent Basis Sets: Principles. *J. Chem. Phys.* **2001**, 115, 9113–9125.

48. Jensen, F.; Erratum: "Polarization Consistent Basis Sets: Principles". *J. Chem. Phys.* **2002**, 116, 3502.

49. Levine, D. S.; Horn, P. R.; Mao, Y.; Head-Gordon, M. Variational Energy Decomposition Analysis of Chemical Bonding. 1. Spin-Pure Analysis of Single Bonds *J. Chem. Theor. Comput.* **2016**, 12, 4812-4820.

50. Levine, D. S.; Head-Gordon, M. Quantifying the Role of Orbital Contraction in Chemical Bonding. *J. Phys. Chem. Lett*. **2017**, 8, 1967-1972.

51. Shao, Y.; Gan, Z.; Epifanovsky, E.; Gilbert, A. T. B.; Wormit, M.; Kussmann, J.; Lange, A. W.; Behn, A.; Deng, J.; Feng, X.; Ghosh, D.; Goldey, M.; Horn, P. R.; Jacobson, L. D.; Kaliman, I.; Khaliullin, R. Z.; Kus, T.; Landau, A.; Liu, J.; Proynov, E. I.; Rhee, Y. M.; Richard, R. M.; Rohrdanz, M. A.; Steele, R. P.; Sundstrom, E. J.; Woodcock, H. L.; Zimmerman, P. M.; Zuev, D.; Albrecht, B.; Alguire, E.; Austin, B.; Beran, G. J. O.; Bernard, Y. A.; Berquist, E.; Brandhorst, K.; Bravaya, K. B.; Brown, S. T.; Casanova, D.; Chang, C. M.; Chen, Y.; Chien, S. H.; Closser, K. D.; Crittenden, D. L.; Diedenhofen, M.; DiStasio, R. J.; Do, H.; Dutoi, A. D.; Edgar, R. G.; Fatehi, S.; Fusti-Molnar, L.; Ghysels, A.; Golubeva-Zadorozhnaya, A.; Gomes, J.; Hanson-Heine, M. W. D.; Harbach, P. H. P.; Hauser, A. W.; Hohenstein, E. G.; Holden, Z. C.; Jagau, T. C.; Ji, H.; Kaduk, B.; Khistyaev, K.; Kim, J.; Kim, J.; King, R. A.; Klunzinger, P.; Kosenkov, D.; Kowalczyk, T.; Krauter, C. M.; Lao, K. U.; Laurent, A.; Lawler, K. V.; Levchenko, S. V.; Lin, C. Y.; Liu, F.; Livshits, E.; Lochan, R. C.; Luenser, A.; Manohar, P.; Manzer, S. F.; Mao, S. P.; Mardirossian, N.; Marenich, A. V.; Maurer, S. A.; Mayhall, N. J.; Neuscamman, E.; Oana, C. M.; Olivares-Amaya, R.; ONeill, D. P.; Parkhill, J. A.; Perrine, T. M.; Peverati, R.; Prociuk, A.; Rehn, D. R.; Rosta, E.; Russ, N. J.; Sharada, S. M.; Sharma, S.; Small, D. W.; Sodt, A.; Stein, T.; Stuck, D.; Su, Y. C.; Thom, A. J. W.; Tsuchimochi, T.; Vanovschi, V.; Vogt, L.; Vydrov, O.; Wang, T.; Watson, M. A.; Wenzel, J.; White, A.; Williams, C. F.; Yang, J.; Yeganeh, S.; Yost, S. R.; You, Z. Q.; Zhang, I. Y.; Zhang, X.; Zhao, Y.; Brooks, B. R.; Chan, G. K. L.; Chipman, D. M.; Cramer, C. J.; Goddard, W. A.; Gordon, M. S.; Hehre, W. J.; Klamt, A.; Schaefer, H. F.; Schmidt, M. W.; Sherrill, C. D.; Truhlar, D. G.; Warshel, A.; Xu, X.; Aspuru-Guzik, A.; Baer, R.; Bell, A. T.; Besley, N. A.; Chai, J. D.; Dreuw, A.; Dunietz, B. D.; Furlani, T. R.; Gwaltney, S. R.; Hsu, C. P.; Jung, Y.; Kong, J.; Lambrecht, D. S.; Liang, W.; Ochsenfeld, C.; Rassolov, V. A.; Slipchenko, L. V.; Subotnik, J. E.; Van Voorhis, T.; Herbert, J. M.; Krylov, A. I.; Gill, P. M. W.; Head-Gordon. Advances in Molecular Quantum Chemistry Contained in the Q-Chem 4 Program Package. *Mol. Phys.* **2015**, 113, 184–215.

52. Ibrahim, Y.; Alsharaeh, E.; Meot-Ner, M.; El-Shall, M. S.; Scheiner, S. Stepwise Hydration of Ionized Aromatics, Energies, Structures of the Hydrated Benzene Cation, and the Mechanism of Deprotonaion Reactions, *J. Am. Chem. Soc*. **2005**, 127, 7053-7064.

53. Hamid, A. M.; El-Shall, M. S.; Hilal, R.; Elroby, S.; Aziz, S. G. Unconventional Hydrogen Bonding to Organic Ions in the Gas Phase. Stepwise Association of Hydrogen Cyanide with the Pyridine and Pyrimidine Radical Cations and Protonated Pyridine, *J. Chem. Phys*. **2014**, 141, 054305.
54. Mesleh, M. F.; Hunter, J. M.; Shvartsburg, A. A.; Schatz, G. C.; Jarrold M. F. Structural Information from Ion Mobility Measurements: Effects of the Long-Range Potential, *J. Phys. Chem.* **1996**, 100, 1682.

55. Behn, A.; Zimmerman, P. M.; Bell, A. T.; Head-Gordon, M. Efficient Exploration of Reaction Paths via a Freezing String Method. *J. Chem. Phys*. **2011**, 135, 224108.

TOC Graphic
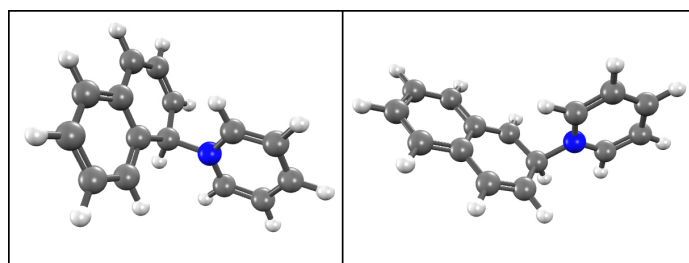
Pyridine attacks the naphthalene radical cation to form a distonic heterodimer resulting in a hybridization change from sp^2 to distorted sp^3 at the site of the attack.